Supplementary Information for

Hyperdoped silicon photodetectors enable room-temperature computational SWIR imaging at 1550 nm

CONTENTS

Supplementary Table 2

Supplementary Text 3

Supplementary Text 1. Single-pixel imaging experiment 3

Supplementary Text 2. Fabrication and selection of photodetectors 4

Supplementary Text 3. Origin of improved performance in ULH-processed device 6

Supplementary Text 4. Stray lights affected dark I–V measurement 7

Supplementary Text 5. Calculation of linear dynamic range (LDR) 8

Supplementary Text 6. Calculation of normalized photocurrent 8

Supplementary Text 7. Calculation of imperial −3 dB cutoff frequency 8

Supplementary Text 8. Noise measurement and specific detectivity determination 9

Supplementary Text 9. Calculation of specific detectivity from I–V measurement and limitation 11

Supplementary Reference 11

SUPPLEMENTARY TABLE

Table S1. Comparison of room-temperature hyperdoped-silicon-based photodetectors operating at 1550 nm (When values at 1550 nm are unavailable, the closest reported wavelength is given in parentheses. J – dark current density, P – light power density, R – responsivity, LDR – linear dynamic range, D* – specific detectivity, τ_r/τ_f – rise/fall times).

Material	Size	Bias	I_{dark}	J (mA/cm2)	P	R	LDR	D*	τ_r/τ_f
Si:S (This work)	**7×7 mm²**	**5 V**	**146.5 µA**	**0.299**	**4.87 mW 15.9 µW**	**14.5 mA/W**	**59.4 dB**	**1.59×10⁹ Jones 1.91×10⁹ Jones**	**166 µs / 186 µs**
Si:Te [1]	140×450 nm² (lateral waveguide incident)	−9 V	≈ 2 µA	-	125 nW	0.56 A/W	33.7 dB	(not able to determine due device structure)	(59 ps from RC estimation)
Si:Te [2]	≈5 mm²	0 V	-	-	20 mW cm⁻²	0.3 mA/W	-	9.2 × 10⁸ Jones	39 µs / 42 µs
Si:Ar [3]	5×5 mm²	12 V	≈ 5 mA	20	3.16 mW	1.28 A/W	-	(1.14 × 10¹⁰ Jones @1310 nm)	-
Si:Ti [4]	1×1 cm²	1 mA	-	1	-	34 mV/W	-	1.7 × 10⁴ Jones	-
Si:Se [5]	≈5 mm²	−1 V	57.3 µA	0.229	35 mW	72 µA/W	≈ 27.3 dB	-	7 ns / 23 ns
Si:Ti/DLC [6]	1 mm²	0 V	-	-	63 mW	2.34 µA/W	-	1.16 × 10⁸ Jones	5 ms / 3 ms
Si:Zn/Gr [7]	-	−3 V – 0 V	< 1 µA	-	2 mW	1.6 mA/W	-	1.56×10⁷ Jones	1.4 ms
Si:He&Ar [8]	-	12 V	12.5 mA	-	-	350 mA/W	-	2.78×10⁹ Jones	(74 µs / 82 µs @1310 nm)
Si:S [9]	5×3 mm²	−20 V	(7.8 µA @−5 V)	(0.052 @−5 V)	-	0.8 A/W	-	-	(0.65 ms / 2.13 ms @632 nm)
Si:Au [10]	1×1 mm²	−5 V	≈ 1.5 µA	0.15	-	11.6 µA/W	-	-	-
Si:Te [11]	-	−2 V	-	-	-	56.8 mA/W	-	-	-
Si:Ag [12]	7×7 mm²	−3 V	≈ > 50 µA	≈ > 0.102	-	65 mA/W	(41.4 dB @1310 nm)	-	(75 µs @1310 nm)
Si:Er&O [13]	200/600 µm donut	2 V	5 µA	0.442	-	(165 µA/W @1310 nm)	-	(1.39×10⁹ Jones @1310 nm)	(14 ms / 12 ms @1310 nm)
Si:Ag/Gr [14]	100 µm channel width (FET)	0.3 V	~ 5 mA	-	-	≈ 92 mA/W (from EQE=7.37%)	(≈ 48.5 dB @1342 nm)	-	(122 µs /131 µs @1342 nm)

SUPPLEMENTARY TEXT

Supplementary Text 1. Single-pixel imaging experiment

While the comprehensive architecture of the same single-pixel imaging (SPI) system is described elsewhere[15], here we outline the specific configurations crucial to the present measurements. The light sources used for imaging included a 1550 nm infrared laser (ThorLabs FPL1009S) and a visible-wavelength LED (Thorlabs MNWHL4) combined with red, green, and blue (RGB) optical filters (whose transmittance spectra were shown in **Fig.S1**). Test objects consisted of a glass slide with a gold film patterned with a kangaroo image and a color photographic slide containing a rainbow lorikeet (a parrot) image.

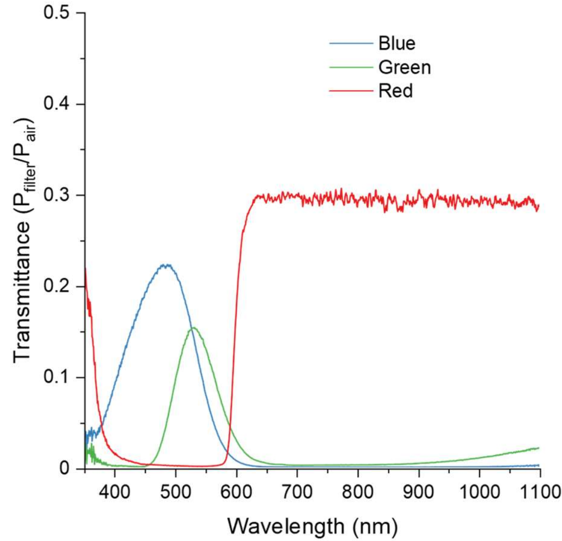

Fig. S1 | Measured transmittance spectra of the red, green, and blue optical filters, referenced to air.

As shown in **Fig.1a**, for SWIR imaging, the 1550 nm laser was collimated and directed onto the object via a flip mirror. The transmitted light was imaged by a camera lens (Nikon, focal length 60 mm) onto a DMD (V-7000, Vialux) at normal incidence, which imposed a sequence of spatial modulation patterns. The reflected, pattern-encoded beam was then relayed by a camera lens (Pentax, focal length 50 mm) and a microscope objective (Mitutoyo, 50× magnification) onto the hyperdoped silicon photodetector, which converted the incident intensity into a time-varying electrical signal. This signal was amplified by the preamplifier (which also provided the detector bias) and demodulated by a lock-in amplifier (Stanford Research SR830), with the laser intensity simultaneously modulated at 1.5 kHz. The lock-in amplified output voltage was digitized by a 14-bit analog-to-digital converter (ADC) and transferred to a personal computer for image reconstruction. The sampled voltages $\boldsymbol{V} \in \mathbb{R}^N$ corresponded to the circular convolution of the first row of the cyclic sensing matrix $\boldsymbol{\Phi_1} \in \mathbb{R}^N$, with the imaging object vector $\boldsymbol{O} \in \mathbb{R}^N$, scaled by a normalization constant m[16] :

$$\boldsymbol{V} = m * (\boldsymbol{\Phi_1} \circledast \boldsymbol{O}).$$

In our SPI implementation, the cyclic S-matrix patterns were generated using a maximal-length shift-register approach[16], generating a first row of the sensing matrix $\boldsymbol{\Phi_1}$ with a total number pixels of reconstructed image pixels $N = 2^n - 1 = p \times q$, where n was an integer number and p, q defined the dimensions of sampling and image matrices, respectively. During the sampling process, the sensing matrix $\boldsymbol{\Phi_1}$ was first reshaped to a matrix of size $p \times q$ and displayed on the DMD as the first pattern.

Because the sensing matrix was binary, each DMD micromirror turned ‘ON’ when the corresponding matrix element was 1 and ‘OFF’ when it is 0. The ADC then sampled the first voltage value, V_1. For subsequent measurements, the DMD displayed the remaining patterns cyclically.

For visible-light (high-resolution) imaging, the preamplifier output was sent directly to the ADC without lock-in detection or light-source modulation. Although the sampling matrix was defined as 1023 × 1025 pixels, the digital micromirror device (DMD) provides only 1024 × 768 micromirrors. Consequently, the full sampling matrix cannot be physically projected, and the reconstructed image resolution was therefore limited to a maximum of 1023 × 768 pixels. A trigger signal was generated by the DMD upon loading each pattern and was sent to the ADC. Upon receipt of this trigger, sampling of the detector signal was initiated by the ADC. The sampled signals corresponding to each displayed pattern were recorded by the control computer.

The reconstruction exploited the equivalence between circular convolution in the spatial domain and multiplication in the Fourier domain. The Fourier transforms of the sampled voltage sequence and of the first row of the cyclic sensing matrix were first computed. The ratio of these spectra was then evaluated in the Fourier domain, followed by an inverse Fourier transform to obtain the reconstructed image.

Supplementary Text 2. Fabrication and selection of photodetectors

Table S3 summarizes the hyperdoping parameters and ULH fluence used for all fabricated detectors. Following metallization, we screened all 14 hyperdoped silicon devices across both vertical (front-rear) and lateral (front-front) configurations to identify those exhibiting sub-bandgap photoresponse.

Table S3. Laser processing variations and initial responsivity results in front-rear mode for all fabricated devices (*Samples selected for characterization in main text.).

Sample number	Pulse per spot	Hyperdoping fluence (J cm^{-2})	ULH fluence (mJ cm^{-2})	Responsivity (mA/W) @ 1550 nm, −20 V
01	20	0.8	-	<1
02	20	0.8	13	<1
03	20	0.8	14	<1
04	20	0.8	15	2.0
05	20	1.2	-	6.4
06	100	0.4	-	<1
07	100	0.8	-	<1
08	100	1.2	-	<1
09	500	0.4	-	6.6
10	500	0.8	-	3.9
11*	500	1.2	-	3.3
12*	500	1.2	10	3.2
13	500	1.2	15	2.8
14	500	1.2	20	<1

Photoresponsivity measurements were performed at the wafer level using a commercial system (Bentham PVE300) with the light intensity calibrated by a Ge reference detector (Bentham DH-Ge) over the 800–1800 nm range. The samples were contacted using a probe needle on the front side and an Aluminum foil on the back side. An additional SMU (Keysight 2401) was used to directly contact both ends of the front-side contacts to provide the bias voltage. Following reports that increased reverse bias

can enhance photoconductive gain, we performed initial measurements at a reverse bias of 20 V in the vertical configuration. This biasing assumes an n-type hyperdoped region on a p-type substrate. The AC photocurrent signal was pre-amplified by a transformer (Bentham 474) and detected using a lock-in amplifier (Bentham 496).

As shown in **Fig.S2**, while several devices demonstrate clear responsivity beyond the silicon bandgap (> 1100 nm) in the vertical mode (**Fig.S2a**), the signals in the lateral mode remain below the system detection limit (**Fig.S2b**). Furthermore, many devices in vertical mode exhibit a responsivity approximately three orders of magnitude higher at above-bandgap wavelengths (800–1100 nm) compared to 1550 nm. This significant difference explains why the imaging performance in the visible and near-infrared (NIR) regimes remains inherently superior to that achieved at sub-bandgap SWIR wavelengths.

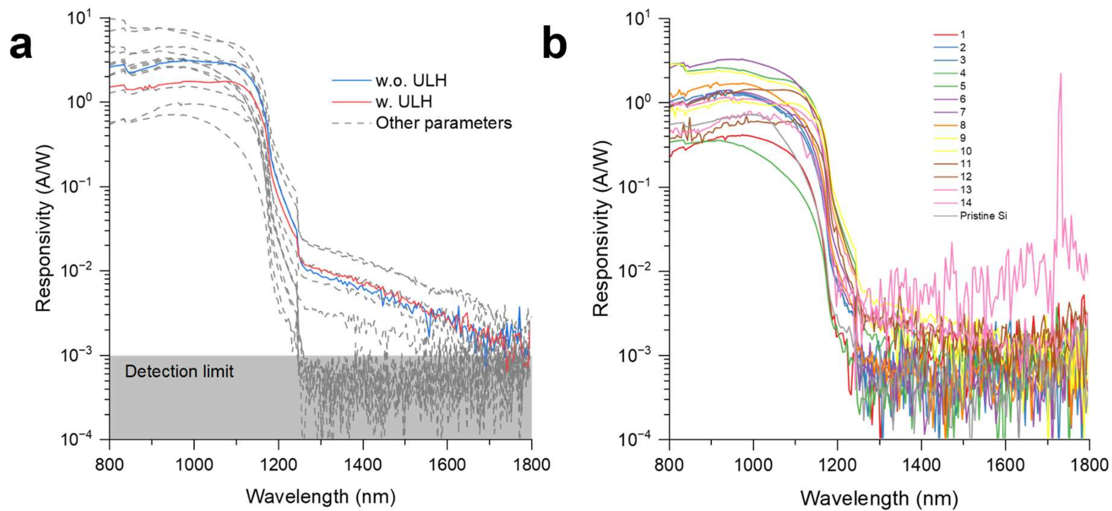

Fig. S2 | a, Spectral responsivity measured in vertical mode under −20 V bias for highlighted devices fabricated with (w.) and without (w.o.) ULH, together with additional process-parameter variations. **b**, Spectral responsivity measured in lateral mode showing no sub-bandgap responsivity with a pristine Si device used as a reference. Data was acquired under a 20 V bias, except for device 4, which was evaluated at 5 V to prevent saturation from excessive dark current.

In lateral mode (**Fig.S2b**), the erratic fluctuations observed in the sub-bandgap regime, particularly the anomalously high values for device 14, are not intrinsic material responses. Rather, they are instrumental measurement artifacts occurring where the noise floor of the setup overwhelms the weak intrinsic photocurrent. The lateral configuration fails to exhibit a sub-bandgap photoresponse mainly due to an overwhelming parasitic dark current flowing through the highly conductive surface layer.

By transitioning to a vertical architecture, the extraction path is redirected across the junction. This not only bypasses the conductive surface shunt but also drastically shortens the carrier transit distance, enabling efficient collection across a large active area. To isolate the influence of the ULH step on device performance, we focused our analysis on a representative pair of detectors fabricated under identical hyperdoping conditions, differing only by the application of the ULH treatment (highlighted in **Fig.S2a**). Although these specific devices do not represent the peak responsivity achieved in this study, they provide a controlled platform to decouple the effects of ULH from other processing variables.

Supplementary Text 3. Origin of improved performance in ULH-processed device

The improved device-level performance (higher sub-bandgap photocurrent and lower dark current, particularly at +5 V) by the ultrafast laser heating (ULH)-processed detector in this work can be understood in the context of the previous systematic study of ULH[17–19] on Si:S hyperdoped layers.

Ultrafast laser hyperdoping of Si in chalcogen-containing atmospheres produces a highly non-equilibrium near-surface region with a substantial fraction of amorphous and heavily disordered silicon and very high local sulfur concentrations in the range of 1 at.%[20]. Raman measurements in prior work show that the as-hyperdoped state contains pronounced amorphous-Si signatures in the 50–200 cm^{-1} and 470–490 cm^{-1} ranges, originating from the rapid resolidification of the laser-induced melt[18]. These amorphous phases are correlated with strong sub-bandgap absorption but also with increased defect scattering and dark (leakage) currents[17]. An "ideal" post-hyperdoping treatment should therefore reduce the non-crystalline fraction while preserving the high sub-bandgap absorptance.

At the atomistic level, defect-engineering models for sulfur-hyperdoped silicon attribute sub-bandgap absorption mainly to deep-level sulfur monomers, which introduce energy states deep within the bandgap and enable sub-bandgap transitions, but do not supply significant free carriers (a source of dark current) at room temperature[17,21–23]. In contrast, shallower sulfur dimers and clusters introduce states closer to the band edges, so they contribute free carriers and dark conductivity but little or no sub-bandgap absorption[17]. Different fabrication and annealing routes are therefore expected to redistribute sulfur among monomer, dimer and cluster configurations, and in doing so jointly tune both the sub-bandgap absorptance and the dark conductivity. Within this framework, an optimal post-processing scheme is one that maximizes the fraction of optically active monomers while minimizing dimer/cluster-related leakage paths.

Systematic post-treatment studies have shown that this balance is delicate. Many purely thermal or top-down etching routes do increase crystallinity, but often at the cost of a noticeable reduction in sub-bandgap absorptance[20], consistent with sulfur diffusion and clustering. By contrast, the combination of controlled thermal diffusion and ULH has been found to move the material into a particularly favorable regime. Previous work[17] shows after a thermal-diffusion step, all ULH-processed samples exhibit higher sub-bandgap absorptance than the as-lasered state, and even thermally "deactivated" samples can have their sub-bandgap absorption reactivated by a subsequent ULH step. At the same time, the same study identifies a group of ULH-treated samples ("Group 2") with comparatively low and thermally stable sheet carrier densities and high carrier mobilities that change only weakly with further diffusion. Mobility analysis indicates that both a low amorphous-silicon fraction and a moderate charge-carrier density are crucial to achieving these high mobilities: reducing amorphous phases lowers defect scattering, while avoiding excessively high doping mitigates free-carrier scattering and dark conduction. On the defect level, these trends are consistent with ULH converting a significant fraction of dimers and clusters into monomers, thereby increasing the monomer concentration and stabilizing the optical and electrical properties against subsequent thermal processing.

The ULH-processed device in this work is designed to operate in the same parameter regime as the favorable ULH-treated group reported previously: it retains strong sub-bandgap absorption around 1550 nm, but with a more crystalline hyperdoped layer, a reduced amorphous fraction and a moderate carrier density, which together yield higher mobility and lower leakage[17] but lower rectification ratio (Fig.2f) with less effective donor density. In contrast, the non-ULH device is expected to preserve more of the as-hyperdoped properties, i.e. a larger amorphous fraction and/or higher free-carrier density, and a less favorable distribution of sulfur among monomer, dimer and cluster states, leading to higher dark current in forward bias, stronger defect-mediated noise, and reduced effective mobility.

Therefore, these material-level trends may provide a consistent explanation for the device-level results reported here: the ULH step drives the hyperdoped region towards a configuration with (i) strong sub-bandgap absorption, (ii) improved crystallinity and reduced amorphous content, and (iii)

moderate carrier density with high mobility. In terms of defect chemistry, this corresponds to a higher fraction of deep-level sulfur monomers and fewer dimer-/cluster-related leakage paths. This combination lowers dark-current-related noise without sacrificing responsivity, so that under forward bias (photoconductive mode) the ULH-processed detector achieves a more favorable balance between gain and noise, and thus higher specific detectivity.

Supplementary Text 4. Stray lights affected dark I–V measurement

Fig. 2e is not fully representative of the intrinsic dark current of the device and is partly an artefact of the initial measurement conditions.

All I–V measurements in **Fig. 2e** were performed in a nominally light-tight enclosure; however, subsequent tests revealed that the measured "dark" current is likely overestimated due to residual background illumination. Possible sources include imperfect light sealing of the enclosure (e.g. small gaps at feedthroughs or door seams), scattered light from the 1550 nm beam path, and visible-wavelength indicator LEDs on the laser source and auxiliary equipment.

We confirmed this observation by re-measuring I–V characteristics (the same sample number 12) by placing the sample in a grounded Faraday cage to further suppress both residual optical background and electromagnetic interference, and the resulting dark current is obviously lower as compared in **Fig.S3**.

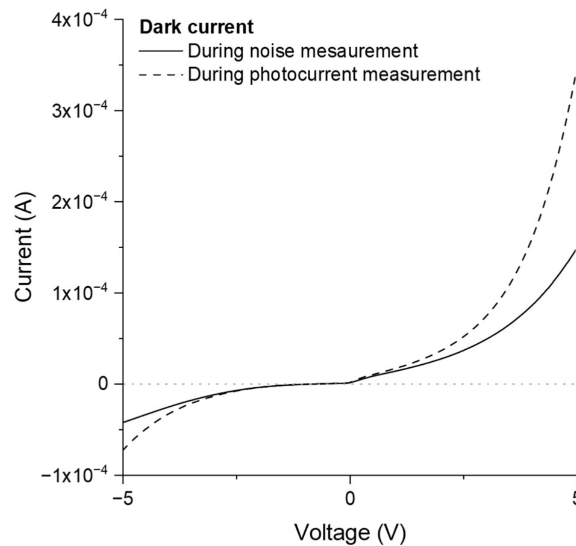

Fig. S3 | Dark current comparison under photocurrent (in a nominal dark box) and noise measurement (in a Faraday cage) setups.

The physical reason for this difference is the hyperdoped-Si detectors exhibit significantly higher responsivity at above-bandgap wavelengths than at 1550 nm (**Fig.S2**). As a result, even weak stray visible lights can generate a measurable photocurrent. This stray-light-induced photocurrent adds to the genuine dark current and leads to an overestimation of the "dark" curve.

Therefore, subtracting photocurrent solely from these DC sweeps using a standard SMU has fundamental limitations for weak sub-bandgap signals, especially when the testing environment contains weak stray lights with above-bandgap wavelengths. Specifically, there are two limitations:

(1) stray lights add to the dark current and therefore an underestimation of detectivity in general. (2) If the dark current is much higher than the photocurrent especially with higher bias voltage, the SMU is forced into a higher range which limits the separation of small signal for high DC current.

Supplementary Text 5. Calculation of linear dynamic range (LDR)

At a forward bias of +5 V, we characterized the photocurrent as a function of incident 1550 nm power over nearly three orders of magnitude, from 4.28 μW to 4.87 mW. The photocurrent I_{ph} was obtained by subtracting the dark current from the total current at each power level.

A power-law fit of the form[24]

$$I_{\text{ph}} \propto P^{\alpha}$$

over the range 4.28 μW–4.01 mW yields $\alpha \approx 0.97$, indicating a nearly linear response across this interval.

Using the minimum (I_{min}) and maximum (I_{max}) photocurrents in the linear response interval, we extract the linear dynamic range[24] as

$$\text{LDR} = 20\log_{10}\left(\frac{I_{\text{max}}}{I_{\text{min}}}\right) \approx 59.4 \text{ dB}.$$

Note that, in this study, the lower bound I_{min} is limited by the available attenuator, so the extracted LDR reflects the measurement window and should be interpreted as an apparent LDR rather than the intrinsic device capability[24].

Supplementary Text 6. Calculation of normalized photocurrent

For the frequency response, we define a normalized photocurrent to compare the relative response under different conditions.

The normalized photocurrent in decibels is given by[24]

$$I_{\text{ph}}(\text{dB}) = 20\log_{10}\left(\frac{I_{\text{ph}}}{I_{\text{ph,max}}}\right),$$

where I_{ph} is the measured photocurrent amplitude at the frequency or preamplifier setting of interest, and $I_{\text{ph,max}}$ is the maximum photocurrent amplitude observed under reference conditions (typically at low modulation frequency and/or at a high-sensitivity setting where the response is not bandwidth-limited).

This normalization removes the absolute scaling of the signal and highlights the relative attenuation as a function of modulation frequency or preamplifier gain. This allows curves taken at different powers or sensitivities to be plotted on the same scale and compared directly.

Supplementary Text 7. Calculation of empirical −3 dB cutoff frequency

The rise (and fall) time recorded from the oscilloscope are defined as the intervals required for the signal to change from 10% to 90% (and 90% to 10%, respectively) of its steady-state amplitude[24].

For a first-order, linear low-pass system, the −3 dB cutoff frequency f_{c} (the frequency at which the output electrical power drops to 50% of its low-frequency value) can be approximately related to the 10–90% rise time t_{r} of the step response via the empirical relation[25]

$$f_c \approx \frac{0.35}{t_r}.$$

We measured $t_r \approx 70$ μs at 0 V and $t_r \approx 166$ μs at +5 V (with similar fall times of 63 and 186 μs, respectively). Substituting these values yields

$$f_c(0V) \approx \frac{0.35}{70 \times 10^{-6}} \approx 5 \text{ kHz},$$
$$f_c(5V) \approx \frac{0.35}{166 \times 10^{-6}} \approx 2.1 \text{ kHz},$$

Although the illumination is square-wave modulated (so each period contains multiple harmonics), the rising and falling edges still approximate step excitations. The 10–90% edge times therefore provide a suitable empirical basis for estimating f_c, and the resulting values are in reasonable agreement with the cutoff frequencies obtained directly from the frequency-response measurements (**Fig. 3f**).

Supplementary Text 8. Noise measurement and specific detectivity determination

This section describes how the current-noise spectra shown in the main text are extracted from time-domain oscilloscope data using FFT-based methods, as schematically shown in **Fig.S4**. The procedure follows standard practice in spectral noise analysis. Note that during noise measurement, the sample was placed in a dark Faraday cage without stray lights and I-V was also measured with a SMU for theoretical noise floor calculation.

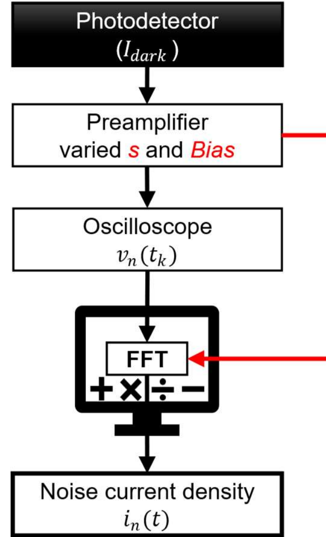

Fig. S4 | Schematic illustrating the procedure used to convert oscilloscope voltage noise to input-referred current-noise density through Fast Fourier Transform (FFT) analysis.

The detector–preamplifier output was connected to a digital oscilloscope, which sampled the noise voltage $v_\text{n}(t_k)$ at 6.25 kS/s over a total acquisition time of 20 s, yielding a discrete time series with $t_k = k\Delta t$, where $\Delta \text{t} = 1/6.25$ kHz is the sampling interval and k is an integer index.

The sampling rate is $F_s = 1/\Delta t$, and the corresponding Nyquist frequency, which sets the highest resolvable frequency, is $f_{\text{Nyq}} = F_s/2$. All spectra are therefore defined on the interval $0 \leq f \leq f_{\text{Nyq}}$. Before spectral analysis, we remove slow drifts that may otherwise contaminate the low-frequency noise. First, the global DC offset is subtracted by replacing $v(t_k)$ with $v'(t_k) = v(t_k) - \langle v \rangle$, where $\langle v \rangle$ is the time-averaged mean. Second, for each analysis segment used in the FFT, we detrend by subtracting a best-fit line, $v_s(n) \rightarrow v_s(n) - (an + b)$. This suppresses slow thermal or bias drift and prevents it from dominating the lowest Fourier bins.

To obtain a statistically reliable estimate of the spectrum, we employ Welch's method[26] rather than a single FFT of the entire record. The detrended time series is divided into K overlapping segments of length L. For each segment we apply a window function, compute its discrete Fourier transform, form

a one-sided power spectral density (PSD), and then average the PSDs over all segments.
If K segments are averaged, the relative standard deviation of the PSD magnitude scales approximately as $\sigma_S/S \approx 1/\sqrt{K}$, so increasing the number of segments reduces the estimator variance.
We use a Hann window,

$$w(n) = 0.5\left[1 - \cos\left(\frac{2\pi n}{L-1}\right)\right], n = 0, \ldots, L-1,$$

and normalize the PSD by the mean-square window power,

$$U = \frac{1}{L}\sum_{n=0}^{L-1} w^2(n),$$

which ensures that the resulting spectrum has the correct units and correctly represents the noise power per unit bandwidth.

For each segment, the one-sided voltage PSD is computed as

$$S_{vv}(f_k) = \frac{2}{F_s\, L\, U} \; | X(f_k) |^2,$$

with units of V^2/Hz, where $X(f_k)$ is the discrete Fourier transform of the windowed segment. The corresponding voltage noise density (amplitude spectral density) is

$$v_n(f) = \sqrt{S_{vv}(f)},$$

with units of V/√Hz. The preamplifier is operated in transimpedance mode with a specified "sensitivity" S in A/V, which corresponds to a nominal transimpedance $Z_t = 1/S$ (V/A). Assuming that the gain is approximately flat over the analysis band, the current-noise density is obtained from

$$i_n(f) = \frac{v_n(f)}{Z_t} = s\, v_n(f),$$

with units of A/√Hz. This is the quantity plotted and analysed in the main text.

The frequency resolution is set by the segment length. For a segment of L points sampled at F_s, the frequency spacing is $\Delta f = F_s/L = 1/T_{\text{seg}}$, where $T_{\text{seg}} = L/F_s$ is the segment duration. In practice, the lowest usable frequency is limited both by the total record length and by detrending; we typically take $f_{\text{min}} \approx \max(1/T_{\text{rec}}, 5\,\Delta f)$, where T_{rec} is the total acquisition time, to avoid bins strongly affected by detrending and windowing. At the high-frequency end, we restrict our analysis to $f_{\text{max}} \approx 0.8\, f_{\text{Nyq}}$, leaving margin below Nyquist to avoid aliasing and window-edge artefacts.

To characterize the noise over a finite frequency band $[f_1, f_2]$, we define a band-integrated current-noise density by integrating the squared spectral density $i_{\text{n}}(f)$ and normalizing by the bandwidth:

$$i_{\text{n,band}} = \sqrt{\frac{1}{f_2 - f_1}\int_{f_1}^{f_2} i_{\text{n}}^2(f)\, \mathrm{d}f}.$$

This quantity has units of A $\text{Hz}^{-1/2}$ and represents the equivalent white-noise density that would produce the same total noise power over the band $[f_1, f_2]$.

In practice, the spectra are approximately flat (white) over the bands of interest, so we estimate $i_{\text{n,band}}$ by taking the average of $i_{\text{n}}(f)$ within the band and using the standard deviation as an uncertainty measure.

Using the sensitivity-dependent $i_{\text{n,band}}(S)$, together with the responsivity $R(S)$ obtained from the photocurrent measurements and the detector active area ($A = 0.49\ \text{cm}^2$) , we compute the specific detectivity

$$D^*(S) = \frac{R(S)\sqrt{A}}{i_{\text{n,band}}(S)}$$

for both high and low incident powers at 1550 nm. In this formulation, D^* is expressed in Jones (cm $\text{Hz}^{1/2}\ \text{W}^{-1}$).

Supplementary Text 9. Calculation of specific detectivity from I–V measurement and limitation

To determine the detector noise floor, we calculate shot noise and thermal (Johnson-Nyquist) noise from dark I–V measurement, and combine these contributions in quadrature:

$$i_{\mathrm{n}} = \sqrt{i_{\mathrm{shot}}^2 + i_{\mathrm{th}}^2},$$

with

$$i_{\mathrm{shot}} = \sqrt{2qI_{\mathrm{dark}}}, i_{\mathrm{thermal}} = \sqrt{\frac{4k_{\mathrm{B}}T}{R_{\mathrm{d}}}}.$$

Here, q is the elementary charge, I_{dark} is the dark current at the bias of interest, k_{B} is Boltzmann's constant, T is the absolute temperature, and R_{d} is the differential resistance extracted from the slope of the dark I–V curve at that bias:

$$R_{\mathrm{d}}(V) = \left|\frac{\mathrm{d}I_{\mathrm{dark}}}{\mathrm{d}V}\right|^{-1}.$$

We note that at lower modulation frequencies, additional noise sources such as $1/f$ noise and trap-related generation–recombination noise[27] may further increase the low-frequency noise. However, in our measurements, detectivity is evaluated for applications involving modulated optical signals in the kHz range, with shot noise becoming dominant at large bias and thus high dark current. Therefore, our approach results in a lower limit of the noise floor when the device operates at white noise plateau.

SUPPLEMENTARY REFERENCE

1. Berencén, Y. *et al.* A high-performance all-silicon photodetector enabling telecom-wavelength detection at room temperature. Preprint at https://doi.org/10.21203/rs.3.rs-5623025/v1 (2025).

2. Wang, M. *et al.* Silicon-Based Intermediate-Band Infrared Photodetector Realized by Te Hyperdoping. *Adv. Opt. Mater.* **9**, (2021).

3. Li, C. *et al.* Record-Breaking-High-Responsivity Silicon Photodetector at Infrared 1.31 and 1.55 μ m by Argon Doping Technique. *IEEE Trans. Electron Devices* **70**, 2364–2369 (2023).

4. García-Hemme, E. *et al.* Room-temperature operation of a titanium supersaturated silicon-based infrared photodetector. *Appl. Phys. Lett.* **104**, (2014).

5. Berencén, Y. *et al.* Room-temperature short-wavelength infrared Si photodetector. *Sci. Rep.* **7**, 43688 (2017).

6. Li, P., Zhang, X., Chen, S., Yu, L. & Feng, S. Investigation of Ti-DLC film for the near infrared photodetector. *Diam. Relat. Mater.* **140**, 110478 (2023).

7. Yu, Z. *et al.* Direct growth of graphene on hyper-doped silicon to enhance carrier transport for infrared photodetection. *Nanotechnology* **35**, 115703 (2024).

8. Zhu, J.-J. *et al.* Enhancing the sub-bandgap photo-response of silicon by inert element co-hyperdoping. *Opt. Lett.* **50**, 367 (2025).

9. Huang, S. *et al.* Black Silicon Photodetector with Excellent Comprehensive Properties by Rapid Thermal Annealing and Hydrogenated Surface Passivation. *Adv. Opt. Mater.* **8**, 1901808 (2020).

10. Mailoa, J. P. *et al.* Room-temperature sub-band gap optoelectronic response of hyperdoped silicon. *Nat. Commun.* **5**, 3011 (2014).

11. Jia, Z. *et al.* Highly responsive tellurium-hyperdoped black silicon photodiode with single-crystalline and uniform surface microstructure. *Opt. Express* **28**, 5239 (2020).

12. Qiu, X., Wang, Z., Hou, X., Yu, X. & Yang, D. Visible-blind short-wavelength infrared photodetector with high responsivity based on hyperdoped silicon. *Photonics Res.* **7**, 351 (2019).

13. Zhang, K. *et al.* Extended infrared responses in Er/O-hyperdoped Si at room temperature. *Opt. Lett.* **46**, 5165 (2021).

14. Wang, Z., Yu, X., Qiu, X., Fu, J. & Yang, D. High-responsivity graphene/hyperdoped-silicon heterostructure infrared photodetectors. *Opt. Laser Technol.* **153**, 108291 (2022).

15. Khaleghi, S. S. M. *et al.* High Pixel Resolution Visible to Extended Shortwave Infrared Single Pixel Imaging with a black Phosphorus-Molybdenum disulfide (bP-MoS2) photodiode. (2025).

16. *Hadamard Transform Optics*. (Elsevier, 1979). doi:10.1016/B978-0-12-330050-8.X5001-X.

17. Paulus, S. *et al.* Defect engineering for improved thermal stability of sulfur hyperdoped silicon. *Mater. Sci. Semicond. Process.* **176**, 108297 (2024).

18. Paulus, S. *et al.* Classification of different post-hyperdoping treatments for enhanced crystallinity of IR-sensitive femtosecond-laser processed silicon. *Semicond. Sci. Technol.* **38**, 024002 (2023).

19. Mc Kearney, P. *et al.* Ultrafast laser heating for controlling the optoelectronic properties of sulfur hyperdoped black silicon. *J. Appl. Phys.* **133**, (2023).

20. Warrender, J. M. Laser hyperdoping silicon for enhanced infrared optoelectronic properties. *Appl. Phys. Rev.* **3**, 031104 (2016).

21. Simmons, C. B. *et al.* Deactivation of metastable single-crystal silicon hyperdoped with sulfur. *J. Appl. Phys.* **114**, (2013).

22. Janzén, E., Stedman, R., Grossmann, G. & Grimmeiss, H. G. High-resolution studies of sulfur- and selenium-related donor centers in silicon. *Phys. Rev. B* **29**, 1907–1918 (1984).

23. Limaye, M. V. *et al.* Understanding of sub-band gap absorption of femtosecond-laser sulfur hyperdoped silicon using synchrotron-based techniques. *Sci. Rep.* **5**, 11466 (2015).

24. Pecunia, V. *et al.* Guidelines for accurate evaluation of photodetectors based on emerging semiconductor technologies. *Nat. Photonics* **19**, 1178–1188 (2025).

25. Sun, J. *et al.* A prototype study of the POLAR front-end electronics. *Nucl. Instrum. Methods Phys. Res. A* **659**, 322–327 (2011).

26. Welch, P. The use of fast Fourier transform for the estimation of power spectra: A method based on time averaging over short, modified periodograms. *IEEE Transactions on Audio and Electroacoustics* **15**, 70–73 (1967).

27. Wang, F., Zhang, T., Xie, R., Wang, Z. & Hu, W. How to characterize figures of merit of two-dimensional photodetectors. *Nat. Commun.* **14**, 2224 (2023).